Optimization of Ca$_{14}$MgSb$_{11}$ through Chemical Substitutions on Sb Sites: Optimizing Seebeck Coefficient and Resistivity Simultaneously

Yufei Hu [ID]**, Kathleen Lee** [ID] **and Susan M. Kauzlarich ***

Department of Chemistry, University of California, One Shields Avenue, Davis, CA 95616, USA; yfhu@ucdavis.edu (Y.H.); Kathy.Lee@jpl.nasa.gov (K.L.)

* Correspondence: smkauzlarich@ucdavis.edu

check for updates

Abstract: In thermoelectric materials, chemical substitutions are widely used to optimize thermoelectric properties. The *Zintl* phase compound, Yb$_{14}$MgSb$_{11}$, has been demonstrated as a promising thermoelectric material at high temperatures. It is *iso*-structural with Ca$_{14}$AlSb$_{11}$ with space group *I*4$_1$/*acd*. Its *iso*-structural analog, Ca$_{14}$MgSb$_{11}$, was discovered to be a semiconductor and have vacancies on the Sb(3) sites, although in its nominal composition it can be described as consisting of fourteen Ca^{2+} cations with one [MgSb$_4$]$^{9-}$ tetrahedron, one Sb$_3$$^{7-}$ linear anion and four isolated Sb^{3-} anions (Sb(3) site) in one formula unit. When Sn substitutes Sb in Ca$_{14}$MgSb$_{11}$, optimized Seebeck coefficient and resistivity were achieved simultaneously although the Sn amount is small (<2%). This is difficult to achieve in thermoelectric materials as the Seebeck coefficient and resistivity are inversely related with respect to carrier concentration. Thermal conductivity of Ca$_{14}$MgSb$_{11-x}$Sn$_x$ remains almost the same as Ca$_{14}$MgSb$_{11}$. The calculated *zT* value of Ca$_{14}$MgSb$_{10.80}$Sn$_{0.20}$ reaches 0.49 at 1075 K, which is 53% higher than that of Ca$_{14}$MgSb$_{11}$ at the same temperature. The band structure of Ca$_{14}$MgSb$_7$Sn$_4$ is calculated to simulate the effect of Sn substitutions. Compared to the band structure of Ca$_{14}$MgSb$_{11}$, the band gap of Ca$_{14}$MgSb$_7$Sn$_4$ is smaller (0.2 eV) and the Fermi-level shifts into the valence band. The absolute values for density of states (DOS) of Ca$_{14}$MgSb$_7$Sn$_4$ are smaller near the Fermi-level at the top of valence band and 5*p*-orbitals of Sn contribute most to the valence bands near the Fermi-level.

Keywords: Zintl; Ca$_{14}$AlSb$_{11}$; polar intermetallic; thermoelectric

1. Introduction

Thermoelectric materials have attracted significant attention as they can improve the efficiency of energy through converting wasted heat into electricity. The efficiency of thermoelectric materials can be evaluated through the figure of merit (*zT*) by Equation (1).
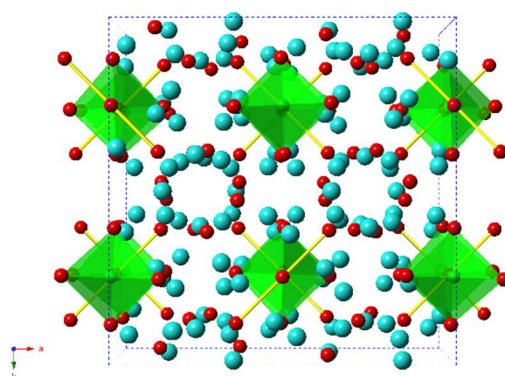
$$zT = \frac{\alpha^2}{\rho\kappa}T \tag{1}$$

In the equation, α is the Seebeck coefficient, ρ is electrical resistivity, *T* is the absolute temperature and κ is thermal conductivity. Defects or tiny amounts of chemical substitutions are important to the optimizations of thermoelectric properties in some typical thermoelectric materials as defects can tune carrier concentrations effectively and adjust the Seebeck coefficient and electrical resistivity. Cationic defects, tuned carrier concentrations and optimized thermoelectric properties were observed in *Zintl* phase compounds [1–3]. Defects can also scatter phonons, make the systems phonon-glass-like and decrease lattice thermal conductivity. The Zn defects in Zn-Sb compounds and Cu defects

in Cu-chalcogenides are essential for decreasing lattice thermal conductivity and tuning of carrier concentrations [4–10]. In some Type-I clathrates, defects have been found in frameworks and the ordering of vacancies are important for the tuning of the Seebeck coefficient, electrical resistivity and thermal conductivity [11–15]. Defects in clathrates can also change the band structure as the bonding and antibonding orbitals of framework elements contribute to the bands near the Fermi-level [11].

Considering the fact that defects are actually replacing atoms with voids, small amounts of chemical substitutions also have similar effects on thermoelectric properties. 1.25% Zn substitutions of IIIA atoms in *p*-type thermoelectric materials $Eu/Sr_5In_2Sb_6$ and $BaGa_2Sb_2$ add a hole in the structure and are able to significantly change the carrier concentrations, therefore changing electrical resistivity and Seebeck coefficient [16–18]. In IV-VI materials, 1–2% of potassium, sodium or thulium doping can improve the thermoelectric properties significantly [19–23]. The benefit of K or Na doping may reside in two aspects. The first one is the change of DOS near the Fermi-level, which can increase the effective mass and lead to an improved Seebeck coefficient. The other benefit is the formation of a *nano*-composite, which can effectively decrease lattice thermal conductivity. More recently, a GeTe-based material with Pb and Bi_2Te_3 doping (3 mol %) was discovered to have a *zT* value of 1.9 at 773K [24]. 1% doping of rare earth elements in TAGS-85 samples increases Seebeck coefficient and therefore leads to larger *zT* values [25,26]. In half-*Heusler* alloys, small amounts of substitutions (1%) can also dramatically (~50%) improve thermoelectric properties [27–30].

The *Zintl* phase compounds, $Yb_{14}MgSb_{11}$ and $Ca_{14}MgSb_{11}$, were reported in 2014 and their thermoelectric properties studied [31]. Both of them have the $Ca_{14}AlSb_{11}$-type of structure (Figure 1 and Table 1), and $Ca_{14}MgSb_{11}$ was found to have vacancies (2.6%) on the isolated Sb(3) sites. These sites are coordinated by Ca^{2+} cations and are shown as the non-bonded Sb atoms in Figure 1. $Yb_{14}MgSb_{11}$ has a *zT* of ~1 at 1075 K while $Ca_{14}MgSb_{11}$ has a semiconductor-like resistivity and a *zT* of 0.32 at 1075 K. Their *iso*-structural analog, $Yb_{14}MnSb_{11}$, has also been discovered as a good thermoelectric material and many studies have been conducted to optimize its thermoelectric properties [2,32]. Samples synthesized by powder metallurgy have slightly larger (~20 Å³ out of ~6000 Å³) unit cell parameters than crystals synthesized by the Sn-flux method based on the refinement of powder X-ray diffraction patterns. This suggests that crystals of $Yb_{14}MnSb_{11}$ synthesized by the Sn-flux method may have small amounts of Yb or Mn vacancies. The smaller resistivity and lower Seebeck coefficient of $Yb_{14}MnSb_{11}$ samples synthesized as crystals are also consistent with the above statements. Further studies show that 1% Te or Ge substitutions on Sb site can significantly alter the thermoelectric properties [33,34].

Figure 1. Unit cell of $Ca_{14}MgSb_{11}$ projected along the *c*-axis. Ca and Sb atoms are represented by blue and red spheres, Sb_3^{7-} ions are shown with yellow bonds and the green tetrahedra are $[MgSb_4]^{9-}$ clusters.

The synthesis and thermoelectric properties of $Ca_{14}MgSb_{11-x}Sn_x$ are systematically investigated. Sn is used to compensate for Sb vacancies and thereby improve the overall thermoelectric properties of $Ca_{14}MgSb_{11}$. Sn has one electron less than Sb, which will tune the carrier concentration and resistivity.

Calculations of the electronic band structures show that Sb(3) sites contribute most near the Fermi-level and therefore substitution of this site may dramatically change the thermoelectric properties [31].

Table 1. Wyckoff positions and atomic coordinates [$\times 10^4$] of atoms for $Ca_{14}MgSb_{11}$.

Atom	Wyckoff Positions	x	y	z
Ca1	32g	9580(2)	9274(2)	8281(1)
Ca2	32g	9771(2)	1264(2)	79(1)
Ca3	16e	3553(2)	0	2500
Ca4	32g	1781(2)	4030(2)	8439(1)
Mg1	8a	0	2500	8750
Sb1	16f	1364(1)	3864(1)	1250
Sb2	32g	37(1)	1100(1)	8059(1)
Sb3 *	32g	8705(1)	9751(1)	9516(1)
Sb4	8b	0	2500	1250

* Sb3 site has 2.6% vacancy.

2. Experimental Section

Reagents. Elemental Ca pieces (99.5%, Alfa Aesar, Tewksbury, MA, USA), Mg turnings (99.98%, Sigma-Aldrich, St. Louis, MO, USA), Sb (99.999%, Alfa Aesar, Tewksbury, MA, USA) and Sn (99.3%, Alfa Aesar, Tewksbury, MA, USA) were used for the synthesis. Ca was cut into small pieces while Mg and Sn were used as received. All elements were handled using inert atmosphere techniques, including an argon filled glovebox with water levels <0.5 ppm.

Synthesis of Powder. Quantitative yield, high purity samples were synthesized through a powder metallurgy method [2]. Melting Sn and Mg together at 600 °C with the ratio 1:2.2 to produce Mg_2Sn as precursor. Samples with the ratio $Ca:Mg:Sb:Mg_2Sn = 14:1.1 \times (1-2x):11-x:x$ (x is the Sn amount) were loaded into a 50 cm^3 tungsten carbide ball mill vial with one large WC ball (diameter = 11 mm) and two small WC balls (diameter = 8 mm). The mixtures of elements were ball milled on a SPEX 8000 M (SPEX SamplePrep, Metuchen, NJ, USA) for one hour and another 30 min after a 30 min break (the 30 min break prevents the reaction mixture from becoming too hot). The fine powder was transferred to a glovebox and then into a niobium tube, which was sealed by arc welding under argon and further jacketed under vacuum in fused silica. $Ca_{14}MgSb_{11-x}Sn_x$ is annealed at 800 °C for 4 days with a heating rate of 30 °C/h [31].

Powder X-ray Diffraction. Samples were examined using a Bruker zero background holder on a Bruker D8 Advance Diffractometer operated at 40 kV and 40 mA utilizing Cu *Kα* radiation. *Kβ* radiation is removed by a Ni filter. WinPLOTR (version Jan 2012, part of the FullProf suite of programs, https://www.ill.eu/sites/fullprof/ University of Rennes 1, Rennes, France) software was used for background subtraction and pattern analysis, and EDPCR 2.00 software (part of the FullProf suite of programs, https://www.ill.eu/sites/fullprof/ University of Rennes 1, Rennes, France) was used to perform Le Bail refinement [35].

Consolidation of Powder. The bulk powder samples were consolidated into dense pellets via a Dr. Sinter Lab Jr. SPS-211Lx or SPS-2050 spark plasma sintering (SPS) system (Sumitomo, Tokyo, Japan) in a 12.7 mm high-density graphite die (POCO) under vacuum (<10 Pa). The temperature was increased from room temperature to 1000–1025 K in 15 min, and remained stable for 5–15 min. When the temperature reached the maximum, the force loaded increased from 3 kN to 5–8 kN. The samples were cooled to room temperature afterwards. The geometrical sample density was larger than 95% of the theoretical density.

Thermal Conductivity. Thermal diffusivity (D) measurement was conducted on the pellet obtained from SPS from 300 K to 1075 K on a Netzsch LFA-457 laser flash unit (Netzsch, Burlington, MA, USA). The pellet surfaces were well polished and coated with graphite. The measurement was conducted under dynamic argon atmosphere with a flow rate of 50 mL/min. Thermal conductivity was calculated using the equation $\kappa = D \times \rho \times C_p$. Room-temperature density was measured from a

volume method and the high-temperature density was derived using thermal expansion data from a previous paper on $Yb_{14}MnSb_{11}$ [36]. The C_p was taken from previous papers, which was measured by differential scanning calorimetry (DSC) [2].

Electrical Transport Properties. A Linseis LSR-3 unit (Linseis, Robinsville, NJ, USA) was employed to measure Seebeck coefficient and electrical resistivity via a four-probe method from 325 K to 1075 K under a helium atmosphere on a bar-shaped sample [37]. The sample which had been previously measured on the LFA instrument was cut into a $2 \times 2 \times 11$ mm bar using a Buehler diamond saw and polished before measurement. The probe distance was 8 mm. For convenience and clarity, Seebeck coefficient, electrical resistivity and thermal conductivity were fit to six-order polynomial functions to calculate zT values. Room-temperature Hall coefficient was measured with a Quantum Design physical property measurement system (PPMS) from 7 T to -7 T by 5-point *ac* technique. Platinum leads were connected to the pressed pellet through silver paste. Carrier concentration was calculated using equation $R_H = -1/ne$ using the average of R_H from different magnetic fields.

Quantum-chemical calculations. Density functional band structure calculations for $Ca_{14}MgSb_{11}$ and $Ca_{14}MgSb_7Sn_4$ were performed using the linear-muffin tin orbital method (TB-LMTO, Stuttgart, Germany, version 47.1b) within the tight binding approximation [38–42]. The density of states (DOS) and band structures were calculated after convergence of the total energy on a dense k-mesh with $12 \times 12 \times 12$ points, with 163 irreducible k-points. A basis set containing $Ca(4s,3d)$, $Mg(3s,3p)$, and $Sb(5s,5p)$ orbitals was employed for a self-consistent calculation, with $Ca(4p)$, $Mg(3d)$ and $Sb(5d,4f)$ functions being downfolded.

3. Results and Discussion

Synthesis and Structure. Mg_2Sn used in the reaction as a precursor was verified by powder X-ray diffraction. There may be very small peaks indicating the existence of unreacted Mg since extra Mg is used in the precursor synthesis. As mentioned in a previous paper, $Ca_{14}MgSb_{11}$ synthesized by powder metallurgy may contain a minor amount of impurity $Ca_{11}Sb_{10}$ and its existence has a limited effect on the thermoelectric properties [31,43]. $Ca_{14}MgSb_{11-x}Sn_x$ ($x = 0.05$ and 0.10) also contained minor amounts of impurities $Ca_{11}Sb_{10}$ while the Le Bail refinement of the powder X-ray diffraction pattern for $Ca_{14}MgSb_{10.80}Sn_{0.20}$ indicates a phase pure sample (Figure 2). These samples are air-sensitive and oxidized rapidly upon exposure, leading to poor quality of powder X-ray diffraction patterns, not suitable for Rietveld refinement. The refined unit cell parameters are listed in Table 2. Generally, the unit cell parameters show a slight increase with the increasing Sn amounts.

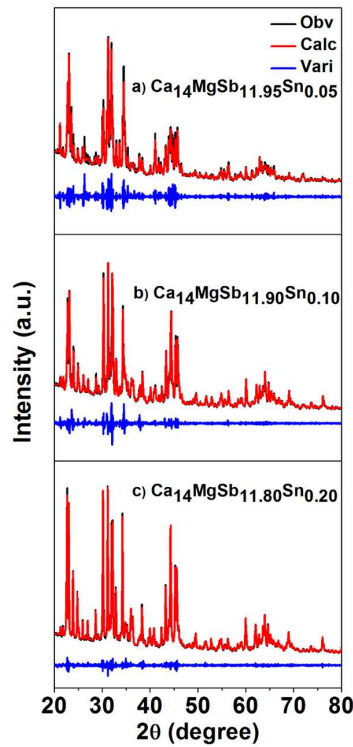**Table 2.** Unit cell parameters from refinement of powder X-ray diffraction patterns.

Sn Amount Used in Synthesis	a (Å)	c (Å)	V (Å^3)
0.00	16.73(1)	22.54(1)	6309(1)
0.05	16.72(1)	22.60(1)	6318(3)
0.10	16.73(1)	22.59(1)	6323(3)
0.20	16.73(1)	22.62(1)	6331(3)

Thermoelectric Properties. Figure 3 shows the results of thermoelectric properties measurement of $Ca_{14}MgSb_{10.95}Sn_x$ ($x = 0.05$, 0.1 and 0.2). The Seebeck coefficient and resistivity of these samples change dramatically with the small changes of Sn compositions. The Seebeck coefficient of $Ca_{14}MgSb_{10.95}Sn_{0.05}$ has a similar trend to that of $Ca_{14}MgSb_{11}$, but the values are much lower. $Ca_{14}MgSb_{10.90}Sn_{0.10}$ and $Ca_{14}MgSb_{10.80}Sn_{0.20}$ have almost the same Seebeck coefficient values, which are slightly higher than the Seebeck coefficient of $Ca_{14}MgSb_{11}$. The linear increase of Seebeck coefficients of $Ca_{14}MgSb_{10.90}Sn_{0.10}$ and $Ca_{14}MgSb_{10.80}Sn_{0.20}$ within the measured temperature region is the most significant change caused by Sn substitutions. The Seebeck coefficient of $Ca_{14}MgSb_{11}$,

which decreases at low temperature and increases at high temperature, is attributed to a combination of increasing temperature and change of carrier concentration based on Equation (2) [19,31].

$$\alpha = \frac{8\pi^2 k_B^2}{3eh^2} m^* T \left(\frac{\pi}{3n}\right)^{\frac{2}{3}} \tag{2}$$

In the equation, k_B is the Boltzmann constant, h is the Planck constant, m^* is the effective mass of carriers and n is carrier concentration. In $Ca_{14}MgSb_{10.90}Sn_{0.10}$ and $Ca_{14}MgSb_{10.80}Sn_{0.20}$, no effect of carrier concentration change is observed in the Seebeck coefficient, which indicates that the substitution of Sn decreases the band gap.

Figure 2. Refinement of the powder X-ray diffraction patterns of (**a**) $Ca_{14}MgSb_{10.95}Sn_{0.05}$, (**b**) $Ca_{14}MgSb_{10.90}Sn_{0.10}$ and (**c**) $Ca_{14}MgSb_{10.80}Sn_{0.20}$.

The resistivity of these samples are semiconductor-like, but the details are different. $Ca_{14}MgSb_{10.95}Sn_{0.05}$ has a larger resistivity than that of $Ca_{14}MgSb_{11}$ at room temperature and a 33% lower resistivity than $Ca_{14}MgSb_{11}$ at high temperatures. The resistivity of $Ca_{14}MgSb_{10.90}Sn_{0.10}$ is higher than the other two samples, especially in the high temperature region. The resistivity of $Ca_{14}MgSb_{10.80}Sn_{0.20}$ follows the expectation, which is lower than that of $Ca_{14}MgSb_{11}$ for the entire temperature region. The activation energy (E_a) can be calculated based on Equation (3) and are listed in Table 3 [31].
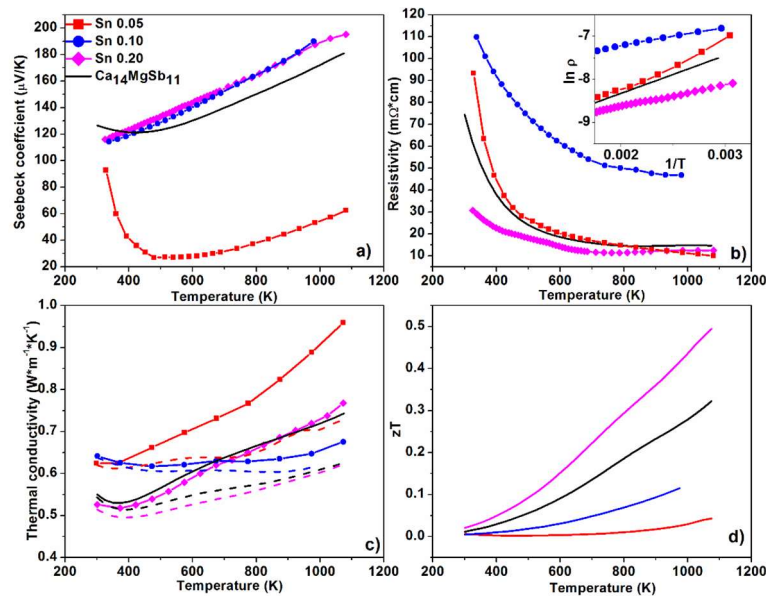
$$ln\ \rho = ln\ \rho_0 + E_a/2k_B T \tag{3}$$

Table 3. Calculated activation energy of $Ca_{14}MgSb_{11-x}Sn_x$.

Composition	Activation Energy (eV)
$x = 0.00$	0.15
$x = 0.05$	0.17
$x = 0.10$	0.08
$x = 0.20$	0.10

It can be seen that the activation energy drops from $x = 0.05$ to $x = 0.10$. The carrier concentration of $Ca_{14}MgSb_{10.80}Sn_{0.20}$ is measured to be $3.5 \times 10^{19}/cm^3$ at room temperature, which is slightly higher than that of $Ca_{14}MgSb_{11}$. Therefore, the carrier concentration has a small change within the three compositions. The Sn substitution of Sb is expected to make $Ca_{14}MgSb_{11}$ more conductive as Sn has one electron less than Sb and this increases the carrier concentration of *p*-type semiconductor $Ca_{14}MgSb_{11}$. However, the carrier concentration change is complex due to the combinations of defects, hole additions caused by Sn doping and the band structure change. The addition of Sn changes the activation energy, which corresponds to the band gap, but this cannot change the intrinsic semiconductor properties of $Ca_{14}MgSb_{11}$.

Figure 3. (**a**) Seebeck coefficient, (**b**) resistivity (insert: *ln ρ* vs. $1/T$ plots), (**c**) thermal conductivity with lattice thermal conductivities shown in dashed lines and (**d**) *zT* values of $Ca_{14}MgSb_{10.95}Sn_{0.05}$, $Ca_{14}MgSb_{10.90}Sn_{0.10}$ and $Ca_{14}MgSb_{10.80}Sn_{0.20}$. In all plots, data for $Ca_{14}MgSb_{11}$ are shown in black curves as references.

The thermal conductivities of $Ca_{14}MgSb_{11-x}Sn_x$ (x = 0.05, 0.10 and 0.20) are listed in Figure 2c. The sample of x = 0.05 has the largest thermal conductivity and sample of x = 0.20 has almost the same thermal conductivity as $Ca_{14}MgSb_{11}$. Lorenz numbers of these samples at different temperatures are calculated using Equations (4) and (5) [4,44].

$$L = \left(\frac{k_B}{e} \right)^2 \frac{3F_0(\eta)F_2(\eta) - 4F_1(\eta)^2}{F_0(\eta)^2} \tag{4}$$

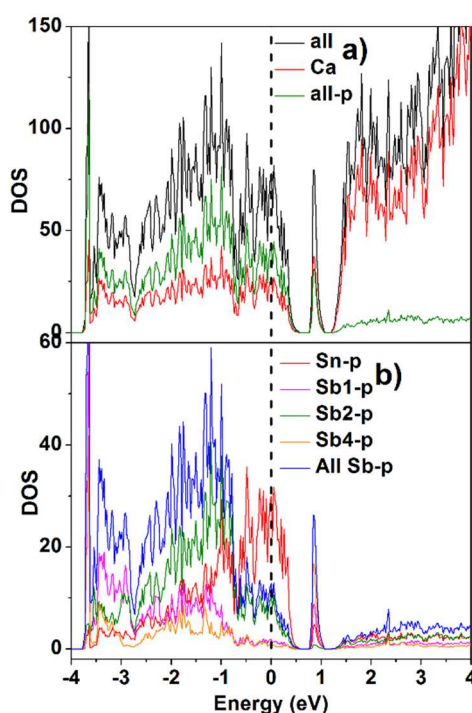$$\alpha = \frac{k_B}{e} \left[\frac{2F_1(\eta)}{F_0(\eta)} - \eta \right] \tag{5}$$

$$\kappa_{lat} = \kappa - \kappa_e = \kappa - L\sigma T \tag{6}$$

In the equations, L is the Lorenz number, η is the reduced Fermi-level, $F_n(\eta)$ is the Fermi-Dirac integral, κ_{lat} is the lattice thermal conductivity and κ_e is electronic thermal conductivity from electrical conductivity. The lattice thermal conductivity can be calculated by subtracting the electronic thermal conductivity from the total thermal conductivity. The calculated lattice thermal conductivity shows that the lattice term contributes the most to the total thermal conductivity and the electronic term has larger contributions at high temperature regions due to the decrease of resistivity. The calculated *zT* values show that $Ca_{14}MgSb_{10.80}Sn_{0.20}$ has the largest maximum *zT* value of 0.49 at 1075 K, which is

53% higher than that of $Ca_{14}MgSb_{11}$ due to optimized resistivity. $Ca_{14}MgSb_{10.95}Sn_{0.05}$ has a maximum *zT* value of 0.04 at 1075 K due to a lower Seebeck coefficient and $Ca_{14}MgSb_{10.90}Sn_{0.10}$ has a maximum *zT* value of 0.12 due to a much larger resistivity.

4. DOS Calculation

The DOS diagram for $Ca_{14}MgSb_7Sn_4$ is shown in Figure 4. This composition is assumed for calculating the DOS of Sn-substituted $Ca_{14}MgSb_{11}$, as the Sb(3) site is assumed to be occupied by Sn. Several reasons support this hypothesis as the Sb(3) site is known to show vacancies and Sb(3) is the isolated Sb^{3-} site with no direct covalent bonding to other atoms, which is the easiest to be substituted. Because of the large unit cell of $Ca_{14}MgSb_{11}$, Sb(3) is assumed to be fully replaced by Sn although actually at most only 5% of Sb(3) is occupied by Sn. Therefore, the composition used in the calculations is $Ca_{14}MgSb_7Sn_4$.

Figure 4. Density of states (DOS) diagram for $Ca_{14}MgSb_7Sn_4$. (**a**) Total DOS together with partial contributions from Ca and 5*p*-orbitals of Sn and Sb (**b**) Partial DOS showing the contributions of only 5*p*-orbitals of Sn and Sb.

The band structure of $Ca_{14}MgSb_7Sn_4$ (Figure 4) has similar features to that of $Ca_{14}MgSb_{11}$ [31]. The Fermi-level falls into the valence band, to which *p*-orbitals of Sb and Sn have dominating contributions. Sn makes the largest contribution at the top of the valence band near the Fermi-level. The conduction band is mainly from orbitals of Ca, especially when energy is >1.2 eV, and there is a sharp peak at the bottom of the conduction band, which originates from the anti-bonding orbitals of the linear Sb_3^{7-} units and orbitals of Ca. The band gap between the top of the valence band (+0.58 eV) and the bottom of the conduction band (+0.78 eV) is 0.20 eV. This value is smaller than the band gap of $Ca_{14}MgSb_{11}$ (0.6 eV) but is similar to the activation energy calculated from resistivity. It is also noticeable that there is an energy gap of 0.15 eV between the sharp peak and the states at higher energy in the conduction band. Compared to $Ca_{14}MgSb_{11}$, $Ca_{14}MgSb_7Sn_4$ has smaller absolute values for the density of states at the top of valence band near the Fermi-level. Therefore, when Sb is replaced by Sn, two major changes happen to the valence band. The first one is the shift of Fermi-level into the valence band and the other one is the decrease of absolute values of DOS near Fermi-level.

In the experimental samples $Ca_{14}MgSb_{11-x}Sn_x$ (x = 0.05, 0.10 and 0.20), the Sn amount is much lower than that used in the calculations for the DOS. Comparing the electronic calculations for $Ca_{14}MgSb_{11}$ and $Ca_{14}MgSb_7Sn_4$, a small decrease of band gap is expected. This is supported by the experimental results. The Seebeck coefficient strongly depends on the density of states at the Fermi-level [19,45,46].

$$S = \frac{\pi^2}{3} \frac{k_B}{q} k_B T \left[\frac{1}{n} \frac{dn(E)}{dE} + \frac{1}{\mu} \frac{d\mu(E)}{dE} \right]_{E=E_F} \tag{7}$$

$$S = \frac{\pi^2}{3} \frac{k_B}{q} k_B T \left\{ \frac{1}{n} \frac{d[g(E) * f(E)]}{dE} + \frac{1}{\mu} \frac{d\mu(E)}{dE} \right\}_{E=E_F} \tag{8}$$

In Equations (7) and (8), μ is the mobility, n is the carrier density, $g(E)$ is density of states and $f(E)$ is Fermi function [19]. In $Ca_{14}MgSb_{11-x}Sn_x$ (x = 0.05, 0.10 and 0.20), as mentioned above, the Fermi level shifts into valence band and the change of DOS at the Fermi level is difficult to determine. Based on the measured Seebeck coefficient, it can be concluded that Fermi-level of $Ca_{14}MgSb_{10.95}Sn_{0.05}$ falls into a valley of DOS and leads to a small Seebeck coefficient, while $Ca_{14}MgSb_{10.9}Sn_{0.1}$ and $Ca_{14}MgSb_{10.8}Sn_{0.2}$ have Fermi-levels with a large DOS and a large Seebeck coefficient. Mobility is inversely related to resistivity by the equation, $1/\rho = \sigma = ne\mu$ (n is carrier density, e is the charge carrier, u is mobility). Mobility depends on the band structure and affects resistivity significantly as the carrier densities for these samples are approximately the same.

5. Summary

$Ca_{14}MgSb_{11-x}Sn_x$ (x = 0.05, 0.1 and 0.2) solid solutions were synthesized by powder metallurgy with Mg_2Sn as precursor. Although the Sn amount in the samples is small (<2%), optimized Seebeck coefficient and resistivity were achieved simultaneously with similar thermal conductivity. This is very rare, as the Seebeck coefficient and resistivity are inversely related with respected to carrier concentration. The Seebeck coefficient of $Ca_{14}MgSb_{10.95}Sn_{0.05}$ has a similar temperature dependence compared with $Ca_{14}MgSb_{11}$, while the Seebeck coefficients of $Ca_{14}MgSb_{10.90}Sn_{0.10}$ and $Ca_{14}MgSb_{10.80}Sn_{0.20}$ linearly increase from room temperature to high temperature, different from the trend of $Ca_{14}MgSb_{11}$. Their resistivity shows semiconductor behavior and the activation energy decreases with Sn amount. The zT value of $Ca_{14}MgSb_{10.80}Sn_{0.20}$ reaches 0.49 at 1075 K, which is 53% higher than that of $Ca_{14}MgSb_{11}$ at the same temperature. The band structure of $Ca_{14}MgSb_7Sn_4$ is calculated to better understand the effect of Sn substitution. The band gap of $Ca_{14}MgSb_7Sn_4$ is 0.2 eV and the Fermi-level shifts into the valence band. $5p$-orbitals of Sn contribute most to the valence bands near Fermi-level at the top of valence band and the overall DOS of $Ca_{14}MgSb_7Sn_4$ are smaller in the valence band compared to $Ca_{14}MgSb_{11}$. The substitution of Sn increases the carrier concentration and decreases both the Seebeck coefficient and resistivity as expected.

Author Contributions: Y.H. and S.M.K conceived and designed the experiments. Y.H. performed the experiments and analyzed the data. K.A.L. contributed to the DOS calculations. Y.H. wrote the first draft of the manuscript; all co-authors contributed to the final version of the manuscript.

References

1.   Pomrehn, G.S.; Zevalkink, A.; Zeier, W.G.; van de Walle, A.; Snyder, G.J. Defect-Controlled Electronic Properties in AZn_2Sb_2 Zintl Phases. *Angew. Chem. In. Ed.* **2014**, *53*, 3422–3426. [CrossRef] [PubMed]

2.   Grebenkemper, J.H.; Hu, Y.; Barrett, D.; Gogna, P.; Huang, C.-K.; Bux, S.K.; Kauzlarich, S.M. High Temperature Thermoelectric Properties of $Yb_{14}MnSb_{11}$ Prepared from Reaction of MnSb with the Elements. *Chem. Mater.* **2015**, *27*, 5791. [CrossRef]

3.   Zevalkink, A.; Zeier, W.G.; Cheng, E.; Snyder, J.; Fleurial, J.-P.; Bux, S. Nonstoichiometry in the Zintl Phase $Yb_{1-\delta}Zn_2Sb_2$ as a Route to Thermoelectric Optimization. *Chem. Mater.* **2014**, *26*, 5710. [CrossRef]

4.   Toberer, E.S.; Cox, C.A.; Brown, S.R.; Ikeda, T.; May, A.F.; Kauzlarich, S.M.; Snyder, G.J. Traversing the Metal-Insulator Transition in a Zintl Phase: Rational Enhancement of Thermoelectric Efficiency in $Yb_{14}Mn_{1-x}Al_xSb_{11}$. *Adv. Funct. Mater.* **2008**, *18*, 2795. [CrossRef]

5.   Toberer, E.S.; Rauwel, P.; Gariel, S.; Taftø, J.; Jeffrey Snyder, G. Composition and the Thermoelectric Performance of β-Zn_4Sb_3. *J. Mater. Chem.* **2010**, *20*, 9877. [CrossRef]

6.   Snyder, G.J.; Christensen, M.; Nishibori, E.; Caillat, T.; Iversen, B.B. Disordered Zinc in Zn_4Sb_3 with Phonon-glass and Electron-crystal Thermoelectric Properties. *Nat. Mater.* **2004**, *3*, 458. [CrossRef] [PubMed]

7.   He, Y.; Zhang, T.; Shi, X.; Wei, S.H.; Chen, L. High Thermoelectric Performance in Copper Telluride. *NPG Asia Mater.* **2015**, *7*, e210. [CrossRef]

8.   He, Y.; Day, T.; Zhang, T.; Liu, H.; Shi, X.; Chen, L.; Snyder, G.J. High Thermoelectric Performance in Non-Toxic Earth-abundant Copper Sulfide. *Adv. Mater.* **2014**, *26*, 3974. [CrossRef] [PubMed]

9.   Ge, Z.H.; Zhang, B.P.; Chen, Y.X.; Yu, Z.X.; Liu, Y.; Li, J.F. Synthesis and Transport Property of $Cu_{1.8}S$ as a Promising Thermoelectric Compound. *Chem. Commun.* **2011**, *47*, 12697. [CrossRef] [PubMed]

10.   Liu, H.; Shi, X.; Xu, F.; Zhang, L.; Zhang, W.; Chen, L.; Li, Q.; Uher, C.; Day, T.; Snyder, G.J. Copper Ion Liquid-like Thermoelectrics. *Nat. Mater.* **2012**, *11*, 422. [CrossRef] [PubMed]

11.   Kaltzoglou, A.; Fässler, T.; Christensen, M.; Johnsen, S.; Iversen, B.; Presniakov, I.; Sobolev, A.; Shevelkov, A. Effects of the Order–disorder Phase Transition on the Physical Properties of $A_8Sn_{44}\square_2$ (A = Rb, Cs). *J. Mater. Chem.* **2008**, *18*, 5630. [CrossRef]

12.   Kaltzoglou, A.; Fässler, T.F.; Gold, C.; Scheidt, E.W.; Scherer, W.; Kume, T.; Shimizu, H. Investigation of Substitution Effects and the Phase Transition in Type-I clathrates $Rb_xCs_{8-x}Sn_{44}\square_2$ ($1.3 \leq x \leq 2.1$) Using Single-crystal X-ray Diffraction, Raman Spectroscopy, Heat Capacity and Electrical Resistivity Measurements. *J. Solid State Chem.* **2009**, *182*, 2924. [CrossRef]

13.   Chung, D.; Hogan, T.; Brazis, P.; Roccilane, M.; Kannewurf, C.; Bastea, M.; Uher, C.; Kanatzidis, M.G. $CsBi_4Te_6$: A High-Performance Thermoelectric Material for Low-Temperature Applications. *Science* **2000**, *287*, 1024. [CrossRef] [PubMed]

14.   Dolyniuk, J.A.; Owens-Baird, B.; Wang, J.; Zaikina, J.V.; Kovnir, K. Clathrate Thermoelectrics. *Mater. Sci. Eng. R* **2016**, *108*, 1. [CrossRef]

15.   Zaikina, J.V.; Kovnir, K.A.; Sobolev, A.V.; Presniakov, I.A.; Prots, Y.; Baitinger, M.; Schnelle, W.; Olenev, A.V.; Lebedev, O.I.; Van Tendeloo, G.; et al. $Sn_{20.5}\square_{3.5}As_{22}I_8$: A Largely Disordered Cationic Clathrate with a New Type of Superstructure and Abnormally Low Thermal Conductivity. *Chem. Eur. J.* **2007**, *13*, 5090. [CrossRef] [PubMed]

16.   Aydemir, U.; Zevalkink, A.; Ormeci, A.; Gibbs, Z.M.; Bux, S.; Snyder, G.J. Thermoelectric Enhancement in $BaGa_2Sb_2$ by Zn Doping. *Chem. Mater.* **2015**, *27*, 1622. [CrossRef]

17.   Chanakian, S.; Aydemir, U.; Zevalkink, A.; Gibbs, Z.M.; Fleurial, J.-P.; Bux, S.; Snyder, G.J. High Temperature Thermoelectric Properties of Zn-doped $Eu_5In_2Sb_6$. *J. Mater. Chem. C* **2015**, *3*, 10518. [CrossRef]

18.   Chanakian, S.; Zevalkink, A.; Aydemir, U.; Gibbs, Z.M.; Pomrehn, G.; Fleurial, J.-P.; Bux, S.; Snyder, G.J. Enhanced Thermoelectric Properties of $Sr_5In_2Sb_6$ via Zn-doping. *J. Mater. Chem. A* **2015**, *3*, 10289. [CrossRef]

19.   Heremans, J.P.; Jovovic, V.; Toberer, E.S.; Saramat, A.; Kurosaki, K.; Charoenphakdee, A.; Yamanaka, S.; Snyder, G.J. Enhancement of Thermoelectric Efficiency in PbTe by Distortion of the Electronic Density of States. *Science* **2008**, *321*, 554. [CrossRef] [PubMed]

20.   Zhang, Q.; Cao, F.; Liu, W.; Lukas, K.; Yu, B.; Chen, S.; Opeil, C.; Broido, D.; Chen, G.; Ren, Z. Heavy Doping and Band Engineering by Potassium to Improve the Thermoelectric Figure of Merit in p-Type PbTe, PbSe, and $PbTe_{1-y}Se_y$. *J. Am. Chem. Soc.* **2012**, *134*, 10031. [CrossRef] [PubMed]

21.   Pei, Y.; LaLonde, A.; Iwanaga, S.; Snyder, G.J. High Thermoelectric Figure of Merit in Heavy Hole Dominated PbTe. *Energy Environ. Sci.* **2011**, *4*, 2085. [CrossRef]

22.   Girard, S.N.; He, J.; Zhou, X.; Shoemaker, D.; Jaworski, C.M.; Uher, C.; Dravid, V.P.; Heremans, J.P.; Kanatzidis, M.G. High Performance Na-doped PbTe-PbS Thermoelectric Materials: Electronic Density of States Modification and Shape-controlled Nanostructures. *J. Am. Chem. Soc.* **2011**, *133*, 16588. [CrossRef] [PubMed]

23.   Zhao, L.D.; Tan, G.; Hao, S.; He, J.; Pei, Y.; Chi, H.; Wang, H.; Gong, S.; Xu, H.; Dravid, V.P.; et al. Ultrahigh Power Factor and Thermoelectric Performance in Hole-doped Single-Crystal SnSe. *Science* **2016**, *351*, 141. [CrossRef] [PubMed]

24. Wu, D.; Zhao, L.D.; Hao, S.; Jiang, Q.; Zheng, F.; Doak, J.W.; Wu, H.; Chi, H.; Gelbstein, Y.; Uher, C.; et al. Origin of the High Performance in GeTe-Based Thermoelectric Materials upon Bi_2Te_3 Doping. *J. Ame. Chem. Soc.* **2014**, *136*, 11412. [CrossRef] [PubMed]

25. Levin, E.M.; Cook, B.A.; Harringa, J.L.; Bud'ko, S.L.; Venkatasubramanian, R.; Schmidt-Rohr, K. Analysis of Ce- and Yb-Doped TAGS-85 Materials with Enhanced Thermoelectric Figure of Merit. *Adv. Funct. Mater.* **2011**, *21*, 441. [CrossRef]

26. Levin, E.M.; Bud'ko, S.L.; Schmidt-Rohr, K. Enhancement of Thermopower of TAGS-85 High-Performance Thermoelectric Material by Doping with the Rare Earth Dy. *Adv. Funct. Mater.* **2012**, *22*, 2766. [CrossRef]

27. Bhattacharya, S.; Pope, A.L.; Littleton, R.T.; Tritt, T.M.; Ponnambalam, V.; Xia, Y.; Poon, S.J. Effect of Sb Doping on the Thermoelectric Properties of Ti-based half-Heusler Compounds, $TiNiSn_{1-x}Sb_x$. *Appl. Phys. Lett.* **2000**, *77*, 2476. [CrossRef]

28. Shen, Q.; Chen, L.; Goto, T.; Hirai, T.; Yang, J.; Meisner, G.P.; Uher, C. Effects of Partial Substitution of Ni by Pd on the Thermoelectric Properties of ZrNiSn-based half-Heusler Compounds. *Appl. Phys. Lett.* **2001**, *79*, 4165. [CrossRef]

29. Appel, O.; Zilber, T.; Kalabukhov, S.; Beeri, O.; Gelbstein, Y. Morphological Effects on the Thermoelectric Properties of $Ti_{0.3}Zr_{0.35}Hf_{0.35}Ni_{1+\delta}Sn$ Alloys Following Phase Separation. *J. Mater. Chem. C* **2015**, *3*, 11653. [CrossRef]

30. Casper, F.; Graf, T.; Chadov, S.; Balke, B.; Felser, C. Half-Heusler Compounds: Novel Materials for Energy and Spintronic Applications. *Semicond. Sci. Technol.* **2012**, *27*, 063001. [CrossRef]

31. Hu, Y.; Wang, J.; Kawamura, A.; Kovnir, K.; Kauzlarich, S.M. $Yb_{14}MgSb_{11}$ and $Ca_{14}MgSb_{11}$—New Mg-Containing Zintl Compounds and Their Structures, Bonding, and Thermoelectric Properties. *Chem. Mater.* **2015**, *27*, 343. [CrossRef]

32. Toberer, E.S.; Brown, S.R.; Ikeda, T.; Kauzlarich, S.M.; Jeffrey Snyder, G. High Thermoelectric Efficiency in Lanthanum Doped $Yb_{14}MnSb_{11}$. *Appl. Phys. Lett.* **2008**, *93*, 062110. [CrossRef]

33. Yi, T.; Abdusalyamova, M.N.; Makhmudov, F.; Kauzlarich, S.M. Magnetic and Transport Properties of Te Doped $Yb_{14}MnSb_{11}$. *J. Mater. Chem.* **2012**, *22*, 14378. [CrossRef]

34. Rauscher, J.F.; Cox, C.A.; Yi, T.; Beavers, C.M.; Klavins, P.; Toberer, E.S.; Snyder, G.J.; Kauzlarich, S.M. Synthesis, Structure, Magnetism, and High Temperature Thermoelectric Properties of Ge Doped $Yb_{14}MnSb_{11}$. *Dalton Trans.* **2010**, *39*, 1055. [CrossRef] [PubMed]

35. Rodríquez-Carvajal, J. Recent Advances in Magnetic Structure Determination by Neutron Powder Diffraction. *Physica B* **1993**, *192*, 55. [CrossRef]

36. Ravi, V.; Firdosy, S.; Caillat, T.; Brandon, E.; Van Der Walde, K.; Maricic, L.; Sayir, A. Thermal Expansion Studies of Selected High-Temperature Thermoelectric Materials. *J. Electron. Mater.* **2009**, *38*, 1433. [CrossRef]

37. Mackey, J.; Dynys, F.; Sehirlioglu, A. Uncertainty Analysis for Common Seebeck and Electrical Resistivity Measurement Systems. *Rev. Sci. Instrum.* **2014**, *85*, 085119. [CrossRef] [PubMed]

38. Andersen, O.K. Linear Methods in Band Theory. *Phys. Rev. B* **1975**, *12*, 3060. [CrossRef]

39. Andersen, O.K.; Jepsen, O. Explicit, First-Principles Tight-Binding Theory. *Phys. Rev. Lett.* **1984**, *53*, 2571. [CrossRef]

40. Andersen, O.K.; Pawlowska, Z.; Jepsen, O. Illustration of the Linear-muffin-tin-orbital Tight-binding Representation: Compact Orbitals and Charge Density in Si. *Phys. Rev. B* **1986**, *34*, 5253. [CrossRef]

41. Nowak, H.J.; Andersen, O.K.; Fujiwara, T.; Jepsen, O.; Vargas, P. Electronic-structure Calculations for Amorphous Solids Using the Recursion Method and Linear Muffin-tin Orbitals: Application to $Fe_{80}B_{20}$. *Phys. Rev. B* **1991**, *44*, 3577. [CrossRef]

42. Lambrecht, W.R.L.; Andersen, O.K. Minimal Basis Sets in the Linear Muffin-tin Orbital Method: Application to the Diamond-structure Crystals C, Si, and Ge. *Phys. Rev. B* **1986**, *34*, 2439. [CrossRef]

43. Brown, S.R.; Kauzlarich, S.M.; Gascoin, F.; Jeffrey Snyder, G. High-temperature Thermoelectric Studies of $A_{11}Sb_{10}$ (A=Yb, Ca). *J. Solid State Chem.* **2007**, *180*, 1414. [CrossRef]

44. Fistul, V.I. *Heavily Doped Semiconductor*; Plenum Press: New York, NY, USA, 1969.

45. Cutler, M.; Mott, N.F. Observation of Anderson Localization in an Electron Gas. *Phys. Rev.* **1969**, *181*, 1336. [CrossRef]

46. Mahan, G.D.; Sofo, J.O. The Best Thermoelectric. *Proc. Natl. Acad. Sci. USA* **1996**, *93*, 7436. [CrossRef] [PubMed]